Supplementary Material:

Spin-orbit torque driven antiferromagnetic oscillator

P. K. Rout,[1] J. Godinho,[1] F. Vilsmeier,[2] R. Salikhov,[3] J. A. Vélez,[4,5] Z. Šobáň,[6] D. Laroze,[7] O. Gomonay,[8] R. M. Otxoa,[9,4] C. H. Back,[2] O. Hellwig,[3,10] and J. Wunderlich[1,6]

[1]*Institute of Experimental and Applied Physics, University of Regensburg, Universitässtrasse 31, 93051 Regensburg, Germany*

[2]*Fakultät fur Physik, Technische Universität München, 85748 Garching, Germany*

[3]*Institute of Ion Beam Physics and Materials Research, Helmholtz-Zentrum Dresden-Rossendorf, Bautzner Landstrasse 400, 01328 Dresden, Germany*

[4]*Donostia International Physics Center, 20018 San Sebastián, Spain*

[5]*Polymers and Advanced Materials Department: Physics, Chemistry, and Technology, University of the Basque Country, UPV/EHU, 20018 San Sebastián, Spain*

[6]*Institute of Physics, Czech Academy of Sciences, Cukrovarnická 10, 162 00, Praha 6, Czech Republic*

[7]*Instituto de Alta Investigación, Universidad de Tarapacá , Casilla 7D, 1000000, Arica, Chile.*

[8]*Institute of Physics, Johannes Gutenberg-University Mainz, 55128 Mainz, Germany.*

[9]*Hitachi Cambridge Laboratory, Cambridge CB3 0HE, United Kingdom*

[10]*Institute of Physics, Chemnitz University of Technology, Reichenhainer Strasse 70, 09107 Chemnitz, Germany*

Supplementary Note 1: Magnetometry

The spin-orbit torque (SOT) driven antiferromagnetic oscillator is based on a nominally compensated in-plane synthetic antiferromagnet (SAF) system with the following structure: Si/ SiO2 (substrate)/ Ta (5nm)/ Py (2nm)/ Ir (0.34nm)/ Py (2nm)/ Pt (5nm). To determine the magnetic property of the SAF system, we performed magnetometry measurements using a commercial Microsense EZ7 vibrating sample magnetometer (VSM) equipped with an electromagnet capable of delivering fields up to 1.8 T. Supplementary Fig. S1 shows the hysteresis loops measured with the magnetic field applied both in-plane (red) and out-of-plane (blue) directions. The measurements reveal that the hard-axis is oriented along the out-of-plane direction, with an anisotropy field of approximately 0.98 T. From the in-plane hysteresis loop, we observe the spin-flip field, defined as the minimum field at which the magnetizations of both ferromagnetic Py layers in the SAF align parallel to each other and to the applied magnetic field, at about 0.5 T. This reflects a strong RKKY exchange coupling between the two Py layers. Finally, the negligible hysteresis observed near zero field indicates that the two ferromagnetic Py layers are nearly identical, resulting in a well-compensated SAF system.

Supplementary Note 2: Anisotropic magnetoresistance (AMR) and Giant magnetoresistance (GMR)

In our SAF, the anisotropic magnetoresistance (AMR) depends on the orientation of the magnetizations in the two ferromagnetic layers relative to the current direction, while the giant magnetoresistance (GMR) response is determined by their relative alignment to each other. To quantify the magnetoresistance, we applied a small direct current $I_{DC} = 50\ \mu A$ through the nano-constriction device and recorded the resulting DC voltage drop using a precision voltmeter while sweeping the magnetic field for two in-plane orientations, $\Phi = 0^o$ and 90^o, where Φ is the azimuthal angle between the magnetic field ($\vec{H}$) and the current direction. Supplementary Fig. S2a shows the percentage change in resistance as a function of magnetic field for two in-plane orientations, $\Phi = 0^o$ and 90^o. The maximum resistance change of approximately 0.2% observed at $\Phi = 90^o$ arises because the AMR and GMR contributions add up when the field drives a rotation and relative twisting of the

sublattice magnetizations. In contrast, when the field is applied along $\Phi = 0^{o}$ deg, the AMR and GMR contributions cancel each other during the field sweep between the spin-flip and spin-flop fields. This demonstrates that in our SAF the AMR and GMR contributions are of comparable magnitude, each amounting to about 0.1%. Supplementary Fig. S2b presents measurements performed at $\Phi = 45^{o}$, where both AMR and GMR contribute simultaneously. In this configuration, sharp resistance variations are observed at fields of approximately ± 50 mT, indicating spin-flop transitions of the SAF. The presence of hysteresis in both the AMR and GMR signals between the spin-flip and spin-flop fields demonstrates the existence of in-plane biaxial anisotropy. This anisotropy most likely originates from the geometric patterning of the nanoconstriction, which defines two easy axes aligned along the constriction edges ($\pm 45^{\circ}$). From these measurements, the biaxial anisotropy field is estimated to be about 5 mT.

Supplementary Note 3: Time resolved magneto-optic Kerr effect (TR-MOKE) imaging of antiferromagnetic domain structure in SAF

Scanning time-resolved magneto-optic Kerr effect (TR-MOKE) is a powerful tool to stroboscopically probe picosecond magnetization dynamics on the micrometer length scale [1, 2]. In our experiments, the magnetization dynamics in the SAF are excited by applying an RF current, where the damping-like spin–orbit fields periodically generate a net magnetization component out of the sample plane. In TR-MOKE measurements, the laser pulse train is locked to the RF signal; therefore, selecting an RF frequency that is an integer multiple of the laser repetition rate provides a tunable phase delay between the laser pulses and the RF excitation. By detecting the polar Kerr effect, we directly measure the oscillating out-of-plane magnetization component at the RF driving frequency induced by the current.

We performed TR-MOKE measurements on a device similar to that used for the SOT oscillation experiments described in the main text, but with a wider, 1 μm constriction. This geometry is sufficiently large to spatially resolve the antiferromagnetic domain structure within the constriction itself. The current-induced damping-like spin–orbit fields produce an out-of-plane net magnetization whose sign depends on the orientation of the Néel vector. Consequently, domains with opposite Néel vector orientations give rise to polar Kerr signals that are phase-shifted by 180^{o}, enabling us to distinguish between oppositely oriented

magnetic domains, which are separated by 180° domain walls.

In Supplementary Fig. S3 a–d, we present maps of both the amplitude and the phase of the polar Kerr signal, recorded while an RF current at 4 GHz was applied to the device. The data were acquired at zero applied magnetic field after first aligning the layer magnetizations parallel using a sufficiently strong (above the spin-flop transition) in-plane magnetic field, oriented either collinear (Supplementary S3a,b) or perpendicular (Supplementary S3c,d) to the bar axis.

The amplitude maps, together with the corresponding phase maps that display abrupt 180° phase shifts at the boundaries between adjacent domains, provide direct evidence of complex antiferromagnetic domain structures separated by 180° Néel domain walls. Notably, these features are observed also within the constricted region of the device, where the detectable SRE signal is generated.

As shown in Supplementary Fig. S4 a–d, applying an additional DC current modifies the antiferromagnetic domain configuration due to SOT-driven domain wall propagation [3]. Interestingly, domain walls in the constriction remain pinned despite the locally enhanced current density, owing to geometrical pinning that reduces the domain-wall energy [4].

We therefore conclude that passing the spin-flip and/or spin-flop transitions toward zero magnetic field can result in the generation of multiple domains, with domain walls remaining pinned in the constriction region. Since in our devices the SRE response originates from the constriction, we attribute the missing SRE resonance signal of Fig. 1 of the main text to domain-wall pinning at the constriction and the resulting cancellation of the SRE signal.

Supplementary Note 4: Anomalous Nernst effect response in the spin rectification effect measurements

The anomalous Nernst effect (ANE) is the thermally driven analogue of the anomalous Hall effect, generating a transverse electric current, $\vec{J_{ANE}} \propto \vec{\Delta T} \times \vec{M}$, from the cross product of a temperature gradient and the magnetization.

In our SAF devices, Joule heating during spin rectification effect (SRE) measurements establishes a vertical temperature gradient toward the substrate. When the applied in-plane magnetic field tilts the magnetizations of the two antiferromagnetically coupled ferromag-

netic layers such that a net magnetization appears with a component perpendicular to the bar, an ANE contribution emerges as a voltage in our open-circuit measurement geometry, adding to the SRE signal. This contribution is maximized at and above the spin-flip transition, where the two antiferromagnetically coupled ferromagnetic layers align parallel, and for magnetic fields applied perpendicular to the bar axis. Consistent with this geometry, Fig. S5a shows the largest ANE generated offset voltage at $\Phi = 90^o$, while Fig. S5b displays its corresponding sinusoidal angular dependence as a function of a rotating magnetic field above the spin-flip transition.

Supplementary Note 5: Chirality of the direct current induced self oscillations in SAF from micromagnetic simulation

In antiferromagnets, self-oscillations can occur for both polarities of the current, with the chirality of the precession determined by the direction of the current [5]. As shown in Fig. 3 (main text), the dependence of the resonant SRE peaks on the direct current polarity correlates with the precession chirality [6]. Specifically, the sign of the SRE signal reverses when the current polarity is reversed, without any dependence on the reversal of the magnetic field polarity. This behavior arises because both the AMR and GMR, which govern the magnetoresistance variations responsible for the SRE response, remain invariant under the reversal of the sublattice magnetizations. Given that the chiralities of the damping-like torque induced precession are opposite for positive and negative current polarities, the observed sign change in the SRE signal is solely attributed to the reversal of the direct current polarity. To further substantiate this behavior, we have conducted a detailed analysis of the phase relationships in the rectified AMR and GMR responses, extracted via FFT at specific frequencies. This analysis was performed for both opposing magnetic field and current polarities during micromagnetic simulations of injection-locked self-oscillations in our SAF system. By examining the phase shifts, we can gain insight into how the chirality of the precession depends on the polarities of the applied magnetic field or current. The GMR response in this case depends on the relative magnetization alignment of the two ferromagnetic Py layers in the SAF, which is described by the tilt angle ($\theta_{tilt} = cos^{-1}(\vec{M}_1.\vec{M}_2/|\vec{M}_1||\vec{M}_1|)$). GMR response is then proportional to $sin^2(\theta_{tilt}/2)$. On the other hand, the AMR is influenced by the relative orientation of the magnetizations

of the two ferromagnetic Py layers with respect to the direction of current flow. The AMR is proportional to $sin^2(cos^{-1}(M_{x_i}/|\vec{M}_i|))$ where $i = 1, 2$ denotes the two ferromagnetic Py layers. To estimate the total AMR contribution from both layers, a parallel resistor model is used. Fig. S6 presents the phase of the rectified GMR response, obtained via FFT for four different injection-locking RF frequencies and for opposite polarities of both the magnetic field and current. It is apparent that for all RF input frequencies, the phase of the rectified GMR response changes by π when the current polarity is reversed. As expected, no phase reversal is observed when the magnetic field polarity is reversed. The phase analysis from the rectified AMR response shows similar results however for certain frequencies the AMR rectification is absent, hence is not shown here.

Supplementary Note 6: Macro-spin modelling of SOT induced complex self-oscillation modes in SAF

To elucidate the underlying dynamics of SAF-system, we make use of the equation of motion for each ferromagnetic layer, $\mathbf{m}_i$ in the presence of interaction fields $\mathbf{H}_i$ given in explicit Landau-Lifshitz-Gilbert equation

$$\frac{\partial \mathbf{m}_i}{\partial t} = -\gamma\mu_0\, \mathbf{m}_i \times \mathbf{H}_{\text{eff}} + \alpha \mathbf{m_i} \times \frac{\partial \mathbf{m_i}}{\partial \mathbf{t}} - \kappa \mathbf{m_i} \times (\mathbf{m_i} \times \hat{\sigma}) - \kappa\beta(\mathbf{m_i} \times \hat{\sigma}), \tag{S1}$$

where γ is the gyromagnetic constant, μ_0 is the permeability of free space, and α is the Gilbert damping coefficient. The normalized magnetic moments are defined as $\mathbf{m}_i = \mathbf{M}_i/M_s$, where M_s is the saturation magnetization. The second term on the right-hand signifies non-conservative dynamics, acting to dampen the magnetization vector towards the direction of the effective field, $\mathbf{H}_{\text{eff}}$, which corresponds to an energy minimum. The effective field $\mathbf{H}_{\text{eff},i} = \mathbf{H}_{\text{ext}} + H_{exc}\mathbf{m}_j + H_{u,z}m_{iz}\hat{z} - H_{u,x}m_{ix}\hat{x}$, where i and j represents each ferromagnetic layer. The third and fourth terms correspond to the induced torque applied at the interface of each ferromagnetic layer. The pre-factor κ, accompanying both the damping-like and field-like components respectively, is $\kappa = \frac{\gamma\hbar\theta_{\text{SH}}}{2edM_{\text{s}}}j$. j is the current density injected along the $\hat{x}$-axis, e is the electron charge, $\hbar$ is the Planck constant, d is the thickness of the magnetic material, β is the relative strength of the field-like contribution, θ_{SH} is the spin Hall angle and $\hat{\sigma} = \text{sgn}(\theta_{\text{SH}})(\vec{j} \times \hat{z})$ is the unit vector direction of the spin accumulation.

In our simulations, we assumed a Gilbert damping constant of $\alpha = 0.01$ for both magnetic layers. The spin Hall angle is $\theta_{\mathrm{SH}} = 0.15$ and the polarization of the spin accumulation is given by $\hat{\sigma} = (0, 1, 0)$, with $\beta = 0$ because the field-like component of the spin-transfer torque is negligible compared to the damping-like component in this system. The magnetic anisotropy has a hard axis directed along the $\hat{z}$-axis with an associated anisotropy field value of $H_{u,z} \approx -1$ T, which promotes the magnetization of each ferromagnetic layer to lie in the xy-planes. Additionally, we assumed some in-plane anisotropy with an easy axis oriented along the $\hat{x}$-direction, with an associated field value of $H_{u,x} \approx 5$ mT. We consider that the saturation magnetization is the same for both layers and equal to $M_s = 7.9 \times 10^5$ A/m. The antiferromagnetic exchange field between the magnetic layers equal to $H_{\mathrm{exc}} = 250$ mT. In order to mimic conditions in the experiment concerning current injection and external applied magnetic fields, we cover a wide range of current density values ranging from 0 up to 1×10^{12} A/m^2 and -50 mT to 50 mT, respectively. The numerical method to solve the coupled equations S1 is the classical fourth order Runge–Kutta method with a fixed time step of $\Delta\tau = 5 \times 10^{-3}$. To avoid unwanted transitory dynamics for the dynamical analysis, we discard a time window corresponding to number of steps. Additionally, further values for $\Delta\tau$ were analyze with analogous results. The Fourier transforms are also used as complementary indicators. All these indicators have been extensively used to characterized the dynamics of non-linear systems [7–10].

Supplementary Fig. S7 presents a comprehensive analysis of the dynamic behavior of the system under varying applied magnetic fields and current densities. Fig. S7a displays a color density plot of the maximum Lyapunov exponent,λ_1, revealing regions of chaotic and stable dynamics as functions of the applied field along the x-axis and the current density. The computation of Lyapunov exponents involves the evaluation of the average exponential rate of separation of nearby trajectories in phase space, mathematically represented as:

$$\lambda = \lim_{t \to \infty} \frac{1}{t} \log \frac{|\delta\vec{x}(t)|}{|\delta\vec{x}(0)|} \tag{S2}$$

where $\delta\vec{x}(0)$ and $\delta\vec{x}(t)$ are the separations between nearby trajectories in the state space at initial time and at time t, respectively [7, 11, 12]. Eq. S2 provides a quantitative measure of how sensitive the system is to small changes in initial conditions, a fundamental characteristic of chaotic systems. Higher values than 0 for λ_1 indicates chaotic behavior, where small

perturbations grow exponentially over time, leading to unpredictable and complex dynamics. Conversely, λ_1=0 or negative values denote stable dynamics, where perturbations decay, and the system tends towards a limit cycle orbit or towards a fixed point respectively. This map allows us for identifying parameter regions where chaotic or stable dynamics are expected. Moreover, it provides us information concerning stable regions for an optimal functioning of the device. From Fig. S7 panel a, we observe first that for certain values of current density and external applied magnetic field the SAF undergoes periodic self-sustained oscillations (λ_1=0), while some chaotic dynamics are also present for a wide range of applied magnetic fields (λ_1>0). We note also a symmetry in the dynamic response when varying the external applied field and the current density directions. Fig. S7 Panel b shows the bifurcation diagram of the y-component of the magnetization of one of the ferromagnetic layer for a current density of $j = 0.5 \times 10^{12}$ A/m^2, highlighting the transition from periodic to chaotic behavior as the applied magnetic field increases. Fig. S7 Panel c provides an enlarged view of the period-doubling process, a well-known route to chaos in the theory of nonlinear dynamical systems. This behavior highlights the rich and complex nature of interactions in synthetic antiferromagnetic systems, providing deep insight into how variations in control parameters can significantly influence the system's dynamics.

Fig. S7 Panel d illustrates the fixed point state, where the magnetic moments after some transient dynamics end up oriented along the effective magnetic field direction, representing a stable equilibrium. The embedded Fourier transform in the xy-plane confirms the absence of significant oscillatory modes, as the signal remains constant without dominant frequencies. This state corresponds in Fig. S7a, to the beige-colored region, indicating that it is the most prevalent state in the system. This region corresponds to negative Lyapunov exponents, indicating the system's stability. Fig. S7 Panel e presents the periodic dynamic state of the magnetic moments $\mathbf{m}_1$ and $\mathbf{m}_2$, where regular oscillations, which we associate to self-sustained oscillations, occur. The associated Fourier transform in the xy-plane shows peaks at discrete frequencies, indicating well-defined oscillatory modes. Fig. S7 Panel f illustrates the chaotic dynamic state of the system. The magnetic moments $\mathbf{m}_1$ and $\mathbf{m}_2$ exhibit complex and non-repetitive behaviors. The embedded Fourier transform in the xy plane reveals a continuous spectrum of frequencies, which is a typical characteristic feature of chaotic systems and represents the existence of multiple oscillatory modes. The Fourier transforms in the xz and yz planes also reflect this complexity, showing dispersed frequency

components in the z and y directions, respectively.

Supplementary Note 7: DC current and magnetic field dependence of self-oscillations measured by SRE in a symmetric nano-constriction

In addition to the spin rectification effect (SRE) detection of DC current-driven self-oscillations observed in our SAF with an asymmetric notch-shaped nano-constriction, we have also measured similar self-oscillations in a symmetric nano-constriction with a slightly larger constriction width (approximately 450 nm), as shown in supplementary Fig. S8a. Supplementary Fig. S8b presents a colormap of the measured V_{SRE} response as a function of both the applied magnetic field and the DC current density. The threshold current density for the onset of auto-oscillations can be clearly identified and is approximately equal to that observed in the asymmetric device, i.e. $\approx 1.3 \times 10^7\ A/cm^2$. This strongly suggests that the emergence of self-oscillations is a DC current-induced effect, as the RF power was kept constant at 15 dBm for both cases. Here again, the positive (blue) and negative (red) signs of the V_{SRE} peaks are exclusively observed for negative and positive DC current polarities, respectively, indicating the associated chiralities of the self-oscillation modes.

We observe similar self-oscillation modes when both the DC current and the applied magnetic field are reversed simultaneously; that is, the oscillation characteristics for negative current and negative field closely resemble those for positive current and positive field. Likewise, a comparable symmetry is observed between the cases of positive current with negative field and negative current with positive field. This behavior reflects the inherent symmetry of spin–orbit torque with respect to current and field reversal and is also evident in our macro-spin simulation explained in the Supplementary Section 6.

The self-oscillation SRE peak at 8 GHz shifts only slightly with increasing DC current density, showing a magnetic field variation of approximately 1 mT. This minor shift can be attributed to a DC current-induced field-like torque, which modifies the total effective magnetic field and consequently causes a slight change in the resonance condition.

Supplementary Note 8: Simulation of current densities and Oersted fields for

the micromagnetic simulation in MuMax3

In the present study, a SAF is positioned between Platinum (Pt) and Tantalum (Ta) layers, each with opposing spin Hall angles. The electrical current densities applied to the Pt and Ta layers generate pure spin currents that are injected into the two ferromagnetic Py layers, with the spin current direction normal to the interface. These spin currents induce SOTs on the antiferromagnetic order of the SAF, leading to the excitation of magnetization dynamics. To model the influence of current-induced SOTs in our SAF nano-constriction device for micromagnetic simulations, we simulate the electrical current densities and the corresponding Oersted fields using COMSOL Multiphysics [13]. In these simulations, a full-scale SAF stack is assumed, with an asymmetric nano-constriction at the center, and a 1 mA electrical current is applied through the SAF stack. For other input currents strength, the current densities and Oersted fields are scaled linearly. Current densities are calculated at both Pt and Ta sites, while Oersted fields are computed at the two Py sites. These results are then estimated on a rectangular mesh, aligned with the micromagnetic simulation domain, and imported into the MuMax3 simulation as input data. The corresponding profiels are shown in Fig. S9 a and b.

[1] Keatley, P. S. *et al.* Direct observation of magnetization dynamics generated by nanocontact spin-torque vortex oscillators. *Phys. Rev. B* **94**, 060402 (2016). URL https://link.aps.org/doi/10.1103/PhysRevB.94.060402.

[2] Hache, T. *et al.* Combined frequency and time domain measurements on injection-locked, constriction-based spin hall nano-oscillators. *Applied Physics Letters* **114**, 102403 (2019). URL https://doi.org/10.1063/1.5082692. https://pubs.aip.org/aip/apl/article-pdf/doi/10.1063/1.5082692/13584038/102403_1_online.pdf.

[3] Godinho, J. *et al.* Antiferromagnetic domain wall memory with neuromorphic functionality. *npj Spintronics* **2**, 1–8 (2024).

[4] Wunderlich, J. *et al.* Influence of geometry on domain wall propagation in a mesoscopic wire. *IEEE Transactions on Magnetics* **37**, 2104–2107 (2001).

[5] Cheng, R., Xiao, D. & Brataas, A. Terahertz antiferromagnetic spin hall nano-oscillator. *Phys. Rev. Lett.* **116**, 207603 (2016). URL https://link.aps.org/doi/10.1103/PhysRevLett.116.207603.

[6] Wang, L. *et al.* Electrical Excitation and Detection of Chiral Magnons in a Compensated Ferrimagnetic Insulator. *Physical Review Letters* **133**, 166705 (2024). URL https://doi.org/10.1103/PhysRevLett.133.166705.

[7] Wolf, A., Swift, J. B., Swinney, H. L. & Vastano, J. A. Determining lyapunov exponents from a time series. *Physica D: nonlinear phenomena* **16**, 285–317 (1985).

[8] Boccaletti, S., Grebogi, C., Lai, Y.-C., Mancini, H. & Maza, D. The control of chaos: theory and applications. *Physics reports* **329**, 103–197 (2000).

[9] Sprott, J. C. *Chaos and time-series analysis* (Oxford university press, 2003).

[10] Wiggers, V. & Rech, P. C. Multistability and organization of periodicity in a van der pol–duffing oscillator. *Chaos, Solitons & Fractals* **103**, 632–637 (2017).

[11] Strogatz, S. H. *Nonlinear Dynamics and Chaos: With Applications to Physics, Biology, Chemistry, and Engineering* (Westview Press, 2015).

[12] Pikovsky, A. & Politi, A. *Lyapunov exponents: a tool to explore complex dynamics* (Cambridge University Press, 2016).

[13] *COMSOL, Inc.* (COMSOL MULTIPHYSICS software).

Figure Captions

Fig. S1 Hysteresis loop of the SAF: Normalized magnetization as a function of the magnetic field H for in-plane (red) and out of plane (blue) directions measured in an unpatterned SAF.

Fig. S2 AMR and GMR in SAF: a), Percentage of change in resistance ($\Delta R/R$) vs. the magnetic field H for two different in-pane orientations of H; $\Phi = 0^{\text{o}}$ and 90^{o} for the patterned SAF. The inset shows the as measured resitance vs. the magnetic field where a constant offset of 445 Ω is subtracted from the data. **b)**, $\Delta R/R$ vs. H for two different sweeping directions and at $\Phi = 45^{\text{o}}$.

Fig. S3 TR-MOKE imaging of antiferromagnetic domain structure: Phase-resolved TR-MOKE images at 4 GHz and zero magnetic field after saturating the sample in two orientations. **a**, Magnitude map with the saturating field parallel to the bar ($\alpha = 0°$). **b**, Phase map corresponding to ($\alpha = 0°$). **c**, Magnitude map with the saturating field perpendicular to the bar ($\alpha = 90°$). **d**, Phase map corresponding to the ($\alpha = 90°$) data. The phase- and magnitude maps are obtained from phase-resolved scans at 4 GHz in which the relative delay between the microwave drive and the laser repetition rate is swept from 0° to 360°, followed by pixel-wise sinusoidal fitting to extract the local magnetization oscillation magnitdue and phase. The dynamic Kerr signal amplitude can be expressed as $\widetilde{\Theta}_K = \Theta_K e^{i\varphi}$, where Θ_K is the magnitude and φ is the phase of the complex dynamic Kerr response.

Fig. S4 DC current induced domain-wall motion: a–d, TR-MOKE images acquired under 4 GHz microwave excitation and zero external magnetic field, while applying a DC current in the sequence of -13 mA, 0 mA, +13 mA and 0 mA respectively. The tr-MOKE signal probes the dynamic out-of-plane component (M_z) of the net magnetization. These scans are performed at a fixed relative delay of 90° between the the microwave drive and

the laser repetition rate.

Fig. S5 Anomalous Nernst effect (ANE) response: a), Measured V_{SRE} as a function of the magnetic field H for different orientations of H relative to the bar (Φ). The input RF frequency in this case is 8 GHz and the power is 15 dBm. **b)**, Average V_{SRE} between H = -0.8 T and -0.6 T as a function of Φ. The solid line corresponds to a sine fit.

Fig. S6 Sign of SRE from micromagnetic simulations: The phase of the GMR response obtained from FFT at a given frequency is plotted for four different injection-locking RF frequencies. The squares and circles correspond to positive and negative magnetic field polarities respectively with a magnitude 45 mT. The red and blue color corresponds to positive and negative polarity of the direct current. The micromagnetic simulation is carried out for $|I_{dc}| = 1.9\ mA > I_{TH}$ and RF current with 0.5 mA peak magnitude for the respective frequencies.

Fig. S7 SAF dynamical response analysis: a), Color density plot of the maximum Lyapunov exponent λ_1 as a function of the applied field along x-axis H^x_{ext} in mT and the current density j in A/m^2. This plot illustrates regions of chaotic behavior ($\lambda_1 > 0$) and stable dynamics ($\lambda_1 = 0$). **b)**, Bifurcation diagram for a current density $j = 0.5 \times 10^{12}$ A/m^2 as a function of H^x_{ext}. This diagram shows the transition from periodic to chaotic behavior as the field increases. **c)**, Enlarged view of the bifurcation diagram highlighting a period-doubling route to chaos. **d)-f)**, Different dynamic states of the system: **d)**, fixed point state indicating a stable equilibrium; **e)**, periodic dynamic state marked as (e) in the bifurcation diagram, showing the transient period before reaching the final periodic state; and **f)**, chaotic dynamic state marked as (f) in the bifurcation diagram, illustrating the complex and unpredictable behavior typical of chaotic systems. The associated FFTs are shown for each component: x in the xy-plane, z in the xz-plane and y in the yz-plane.

Fig. S8 DC current and magnetic field dependence of self-oscillations: a), Scanning electron microscope image of a symmetric nano-constriction device made from SAF showing

the constriction width of 450 nm. **b)**, Dependence of self-oscillation for the device a) on the magnetic field and dc current density is shown as a 2D color-plot. In this case a fixed RF probing current with 8 GHz frequency is applied for the injection-locking of the self-oscillations. The magnetic field is oriented along the bar direction.

Fig. S9 Simulated current densities and Oersted field: a), The magnitude of the lateral current densities in Pt, when a 1 mA direct current is applied across the entire SAF stack, as simulated using COMSOL. **b)**, The corresponding out of plane component of the Oersted field at the Py site.

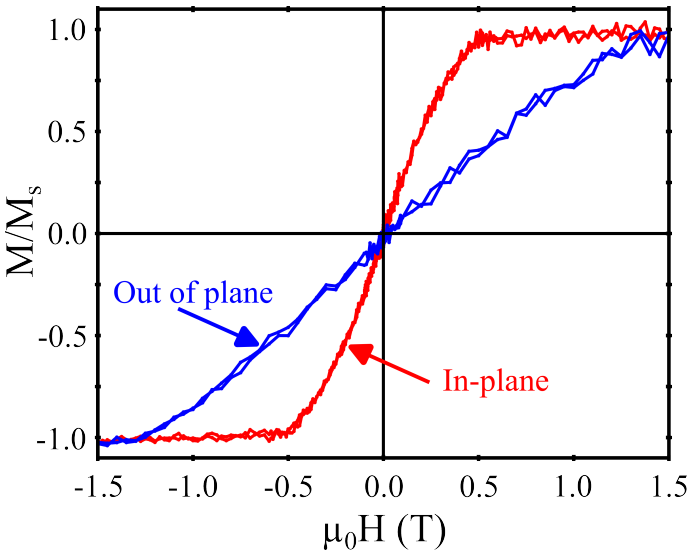

Supplementary Fig. S1.

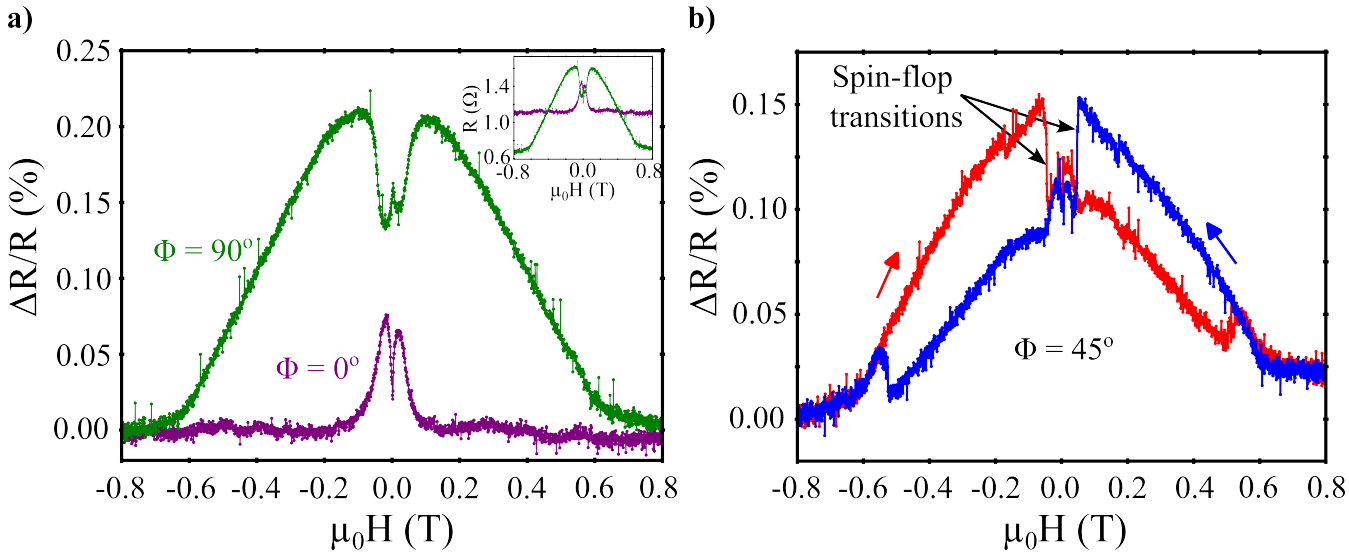

Supplementary Fig. S2.

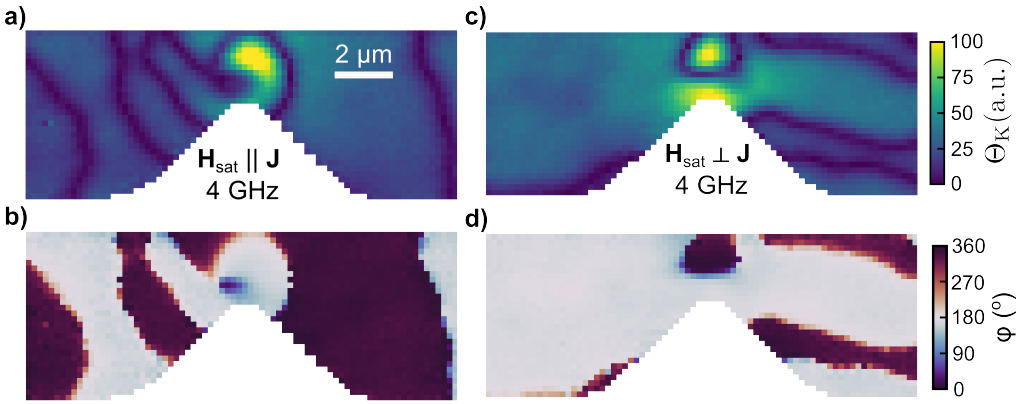

Supplementary Fig. S3.

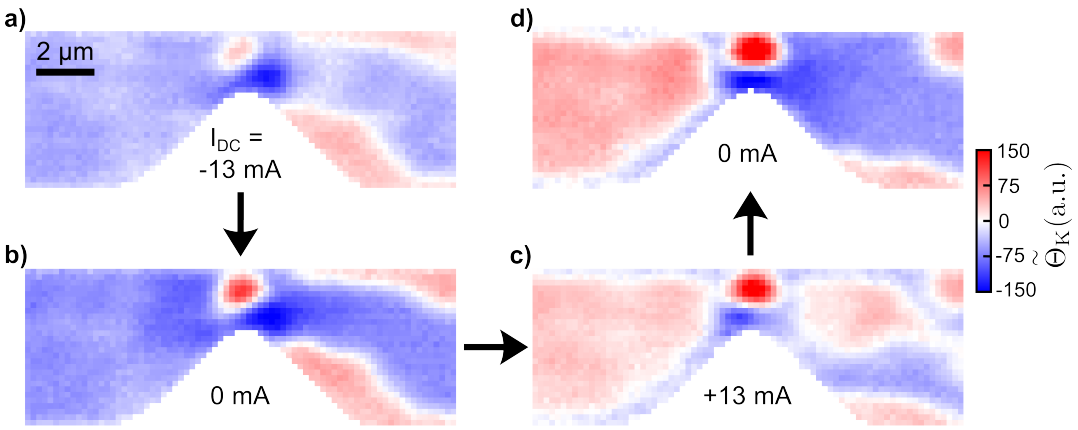

Supplementary Fig. S4.

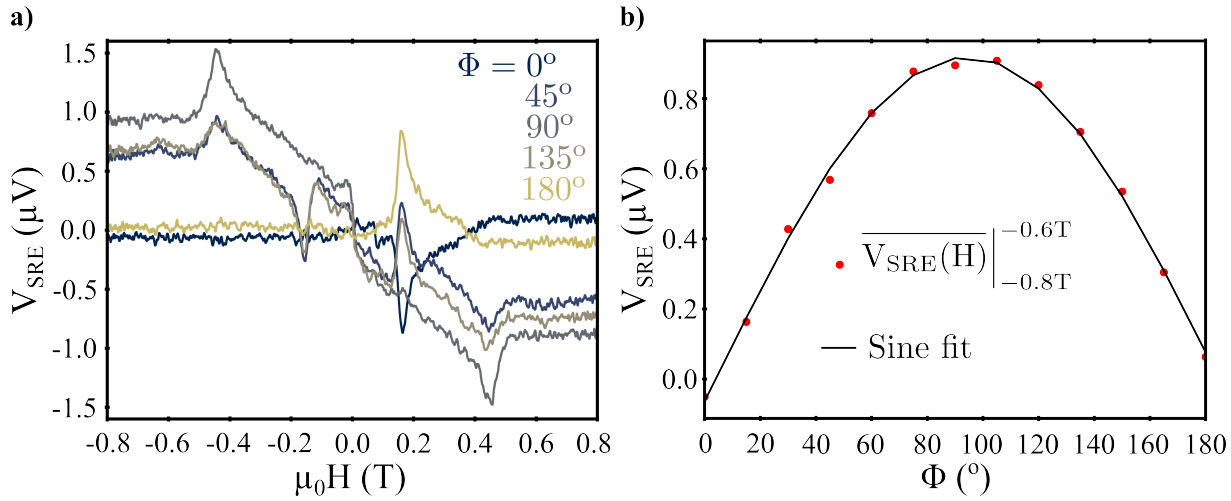

Supplementary Fig. S5.

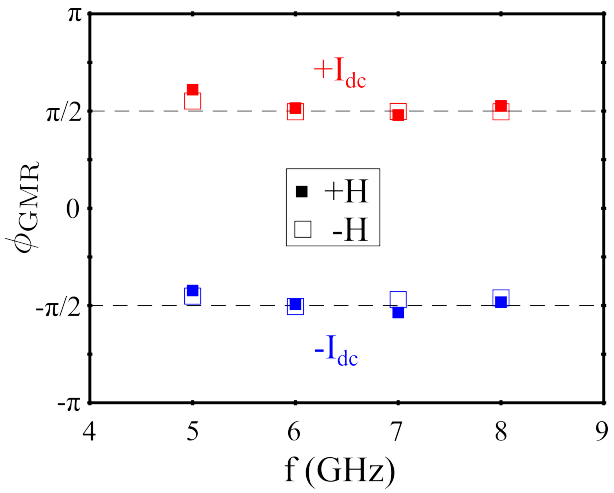

Supplementary Fig. S6.

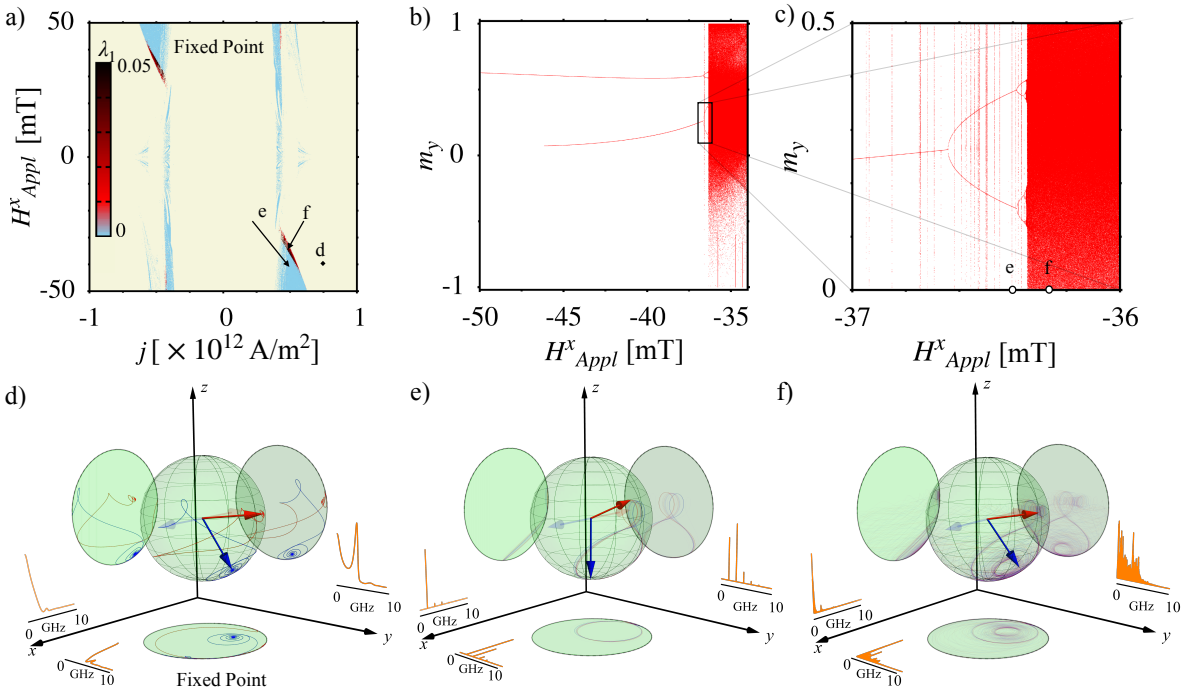

Supplementary Fig. S7.

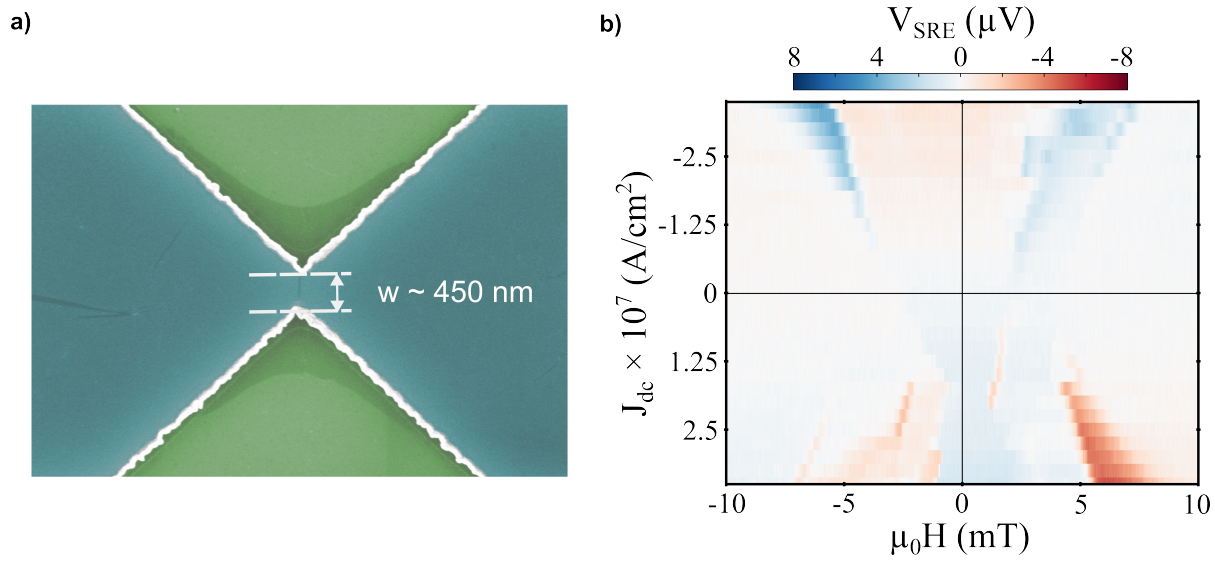

Supplementary Fig. S8.

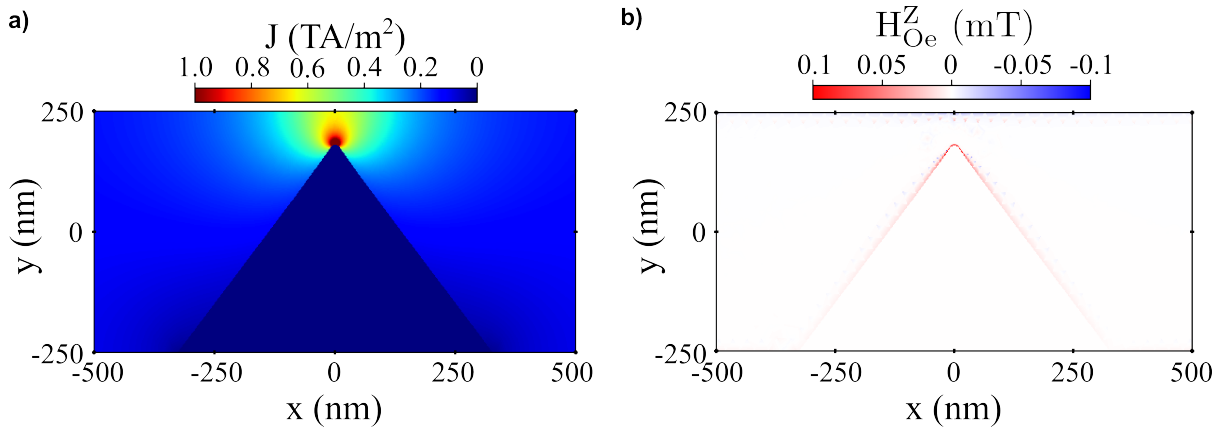

Supplementary Fig. S9.